Electronic Supplementary Information (ESI) for:

Surface morphology-induced spin-crossover-inactive high-spin state in a coordination framework

Shun Sakaida,[a] Kazuya Otsubo,[*a] Ken-ichi Otake,[b] Shogo Kawaguchi,[c] Mitsuhiko Maesato,[a] Susumu Kitagawa[b] and Hiroshi Kitagawa[*ab]

[a.] *Division of Chemistry, Graduate School of Science, Kyoto University, Kitashirakawa Oiwake-cho, Sakyo-ku, Kyoto 606-8502, Japan.*

[b.] *Institute for Integrated Cell-Material Science (iCeMS), Kyoto University, Yoshida, Sakyo-ku, Kyoto 606-8501, Japan.*

[c.] *Japan Synchrotron Radiation Research Institute (JASRI), SPring-8, 1-1-1 Kouto, Sayo-cho, Sayo-gun, Hyogo, 679-5198, Japan.*

*e-mail: kazuya@kuchem.kyoto-u.ac.jp (K.O.); kitagawa@kuchem.kyoto-u.ac.jp (H.K.)

Table of contents

1. Materials and Methods

Materials. All reagents were purchased from Sigma-Aldrich, Kishida Chemical Co., Ltd., and TCI Co., Ltd., and used without further purification. A Au/Cr/Si substrate (20 × 15 × 0.5 mm^3) for film fabrication was prepared by evaporating a chromium buffer layer (5 nm thickness), followed by depositing an Au layer (100 nm thickness), onto a polished silicon wafer (Nilaco Corp.). For annealed samples prior to immersion into the solution of self-assembled monolayer, the substrate surface exposed to thermal annealing by hydrogen burner in air (~2400 K in typical[24]) for each <1 sec for 40 times with an interval for cooling every 5 times, in order to prevent Cr or Si diffusion through Au layer by excessive annealing.[25,26] $[(C_4H_9)_4N]_2[Ni(CN)_4]$, to be used as the LbL solution, was prepared by mixing $[(C_4H_9)_4N]ClO_4$ and $K_2[Ni(CN)_4]$ in ethanol.

Synthesis of bulk-Nipy. The synthesis procedure was similar to that described in earlier works.[15c–15e] Here, 1.56 g $Fe(NH_4)(SO_4)_2{\cdot}6H_2O$ and 1.02 g $K_2[Ni(CN)_4]$ were mixed in 60 ml water, and 3.00 g citric acid was added to the solution. 1,3-Diaminopropane was added dropwise, to yield a yellow transparent solution of $Fe(NH_3)_2[Ni(CN)_4]$. The solution was filled up to 240 ml with water. Vapour diffusion of pyridine afforded a precipitate of a powdered **bulk-Nipy**.

Rietveld refinement of bulk-Nipy. Synchrotron powder diffraction data were measured in the range 2ϑ = 2–78° with a step of 0.006°, using a MYTHEN photon-counting detector installed on the BL02B2 beam line at SPring-8, Japan. The incident X-rays were monochromated to 17.7 keV (λ = 0.7008 Å) with a Si(111) double-crystal monochromator. The initial structure for Rietveld refinement was solved by direct method installed on EXPO2014.[27] The Rietveld structural refinement was performed using the program RIETAN-FP.[28] Final Rietveld refinement result (C14H10FeN6Ni) at 100 K: Orthorhombic, Space Group *Cmmm* (no. 65), a = 7.0930(2) Å, b = 14.8827(4) Å, c

= 6.9183(2) Å, V = 730.32(4) Å^3, Z = 2, R_{wp} = 4.24%, R_e = 2.35%, R_B = 1.86%, R_F = 1.14%, S = 1.80, CCDC reference number 2030844.

Magnetic measurements. The temperature-dependent magnetic susceptibility was measured in a field of 0.1 T using a superconducting quantum interference device (SQUID) magnetometer (MPMS XL, Quantum Design).

Spectroscopic analysis. Variable-temperature Raman spectra measurements were performed using a Jasco NRS-5100 equipped with a 632.8 nm line of 2.4 mW He–Ne laser and a temperature-controlled stage in vacuum (Model S84C, S. T. Japan). The temperature was varied in the range T = 150–373 K at a rate of 5 K/min. Typically, Raman spectra were collected in the 570–1200 cm^{-1} frequency range, twice. The exposure time was typically 10 sec and 100–300 sec for powder and thin-film samples, respectively. Powder samples were placed on the same Au/Cr/Si substrate as used in thin-film fabrication, with adjustment to the same thermal conductivity. The population of spin states was estimated from the ratio of fitting parameters of the pyridine ring breathing mode. The fitting function for Raman spectra intensity (I) was a double-Lorentzian curve with a linear background, where x_c and w represent the frequency at the peak top position and the value of full width at half maximum (FWHM). In the case of LS and HS mixed states, the coefficients of A and B denote the peak areas for the LS and HS states, respectively. The HS fraction γ_{HS} is described as the value of B divided by the summation of A and B.

$$I = \frac{2A}{\pi}\frac{w_1}{4(x-x_{c1})^2+w_1^2} + \frac{2B}{\pi}\frac{w_2}{4(x-x_{c2})^2+w_2^2}$$

To test the applicability of methods reported in an earlier study,[18] the peak intensity of in-plane ring deformation modes around at 642 cm^{-1} (symmetric, I_{v6a}) and at 654 cm^{-1} (antisymmetric, I_{v6b}) were also used to calculate the HS fraction, using I_{v6b} divided by the summation of I_{v6a} and I_{v6b} (see also Fig. S5).

$$I = I_{\nu 6a}\frac{w_1^2}{(x-x_{c1})^2+w_1^2} + I_{\nu 6b}\frac{w_2^2}{(x-x_{c2})^2+w_2^2}$$

Furthermore, the spin transition can be also determined using the cyanide vibration mode (Fig. S4).

Fabrication of film-Nipy. Thin-film fabrication was carried out via the LbL technique at rt, as previously reported.[15c–15e] An as-supplied or annealed Au/Cr/Si substrate was immersed into an ethanol solution of 4-mercaptopyridine (10 mM) overnight to construct a self-assembled monolayer. After rinsing with ethanol, the substrate was alternately soaked in two ethanol solutions of the MOF building block molecules (referred to as 1 cycle): 25 mM of $Fe(BF_4)_2{\cdot}6H_2O$ and 25 mM of $[(C_4H_9)_4N]_2[Ni(CN)_4]$, both containing an excess amount of 100 mM pyridine. Both ethanol solutions were sealed in vials and kept overnight (the colour of the ethanol solution of $Fe(BF_4)_2{\cdot}6H_2O$/pyridine turned transparent yellow). Saturated solutions were prepared for LbL fabrication. Samples of **film-Nipy-nL** (n = 20, 40) were immersed into the two solutions (3 min immersion in each), for up to n cycles. After each immersion, the substrate was rinsed with ethanol.

AFM imaging. AFM images were recorded at rt using the Asylum Research Cypher instrument (Oxford Instruments), equipped with blueDrive photothermal excitation.

Image analysis. Processing of AFM images was carried out using the ImageJ[29] built-in with plug-in capability. For the effective binarization of AFM images, a bandpass filter in FFT command was used to enhance edges and to reduce noise. A watershed segmentation algorithm was applied to the binarized image to separate domains. The counting of domains and measuring of areas were performed using the Analyze Particles command.

Surface X-ray diffraction measurements. Preliminary diffraction data were collected at the BL13XU beam line in SPring-8, Japan. To protect samples from X-ray irradiation

damage, a Rigaku SmartLab X-ray diffractometer with Cu *K*α radiation (λ = 1.541 Å) was used for structural characterization of the obtained films. For in-plane scans, the grazing incidence mode with an incident angle of 0.2° was applied. A 200 diffraction peak FWHM of **film-Nipy** in out-of-plane measurements was used to estimate the crystallite size (average thickness), using Scherrer's equation.

Computational study. Structural optimization and frequency calculations were performed using the Gaussian09W package,[30] using the BP86 functional with the def2-TZVP basis set. To form the initial guess structures (Fig. S23 and S24), the $\{Fe[Ni(CN)_4]\}_\infty$ layer was approximated as Fe^{II} coordinated by four cyanide ligands capped with H atoms (hydrogen cyanide). The Fe–N bond lengths in the initial structures for their LS state were constrained to those in the results of single-crystal analysis for **bulk-Nipy**. For the HS2 state, the $Fe–N_{pyridine}$ bond length was fixed at the intermediate value between those of **bulk-Nipy** in the LS and HS states (2.1125 Å). Total charge of the compound was set to +2. The spin multiplicity was set to singlet (*S* = 0, LS) and quintet (*S* = 2, HS2). Frequency calculations were consequently performed on each optimized structure, to confirm no imaginary frequency and to simulate Raman spectra patterns.

2. Supplementary Figures and Tables

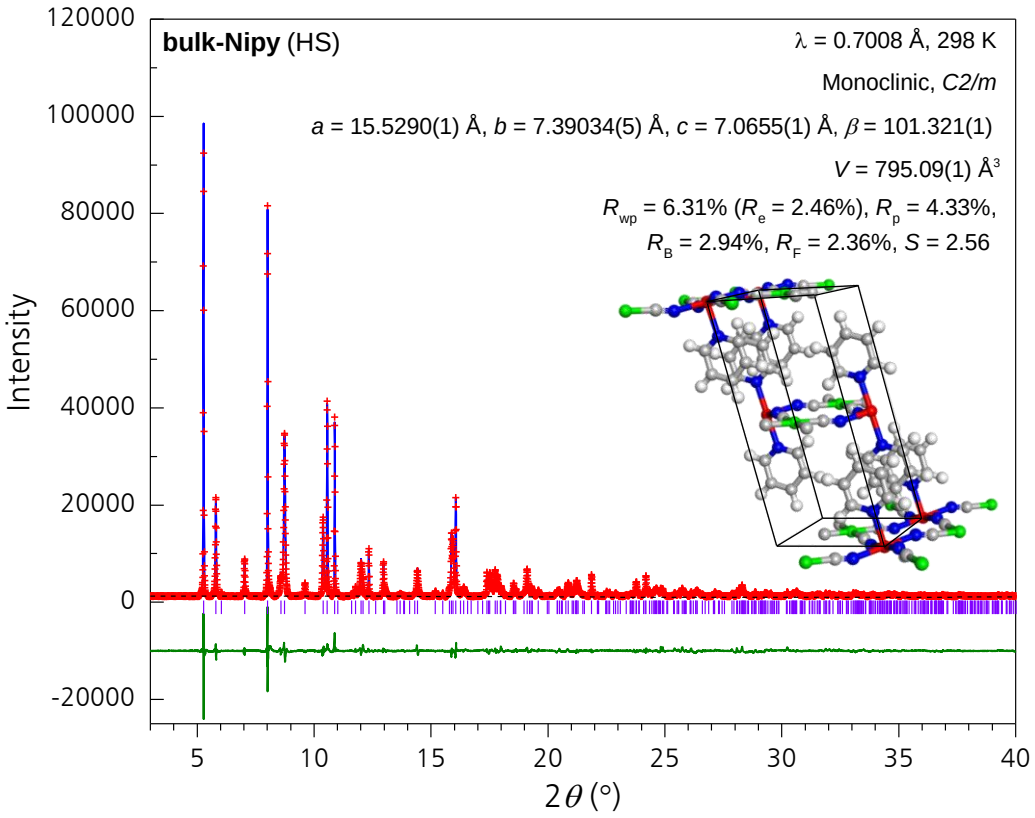

Fig. S1 Rietveld refinement of **bulk-Nipy** structure in HS state. Synchrotron XRD profile of **bulk-Nipy** (red cross) was collected at 298 K. A calculated pattern is represented by a blue line with a background (black dashed line). Magenta bars denote the positions of allowed Bragg reflections. The residual curve (observed minus calculated) is plotted by the below green line. The refined lattice parameters and standard deviations were determined as a = 15.5290(1) Å, b = 7.39034(5) Å, c = 7.0655(1) Å, β = 101.321(1), V = 795.09(1) Å^3. Some constraints were imposed on bond lengths and angles of the pyridine ring. (Inset) A perspective view of the unit cell is shown (monoclinic, *C2*/*m*). Colour code: Fe (red), C (grey), N (blue), Ni (green), H (white).

Table S1 Atomic coordinates and displacement factors for **bulk-Nipy** in HS state (*T* = 298 K).

Atom	Wyckoff position	x	y	z	Site occupancy	U_{iso}
Fe1	2*a*	0	0	0	1	0.020(1)
Ni1	2*d*	0	1/2	1/2	1	0.0058(8)
N1	8*j*	0.0215(3)	0.2111(5)	0.2154(5)	1	0.005(2)
C1	8*j*	0.0088(4)	0.3281(7)	0.3182(7)	1	0.028(3)
N2	4*i*	0.1402(4)	0	−0.015(1)	1	0.018(2)
C2	4*i*	0.1949(7)	0	0.151(2)	1	0.037(4)
C3	4*i*	0.2911(5)	0	0.151(1)	1	0.007(3)
C4	4*i*	0.3200(5)	0	−0.030(1)	1	0.001(3)
C5	4*i*	0.2507(8)	0	−0.205(2)	1	0.023(3)
C6	4*i*	0.1666(6)	0	−0.194(1)	1	0.029(4)

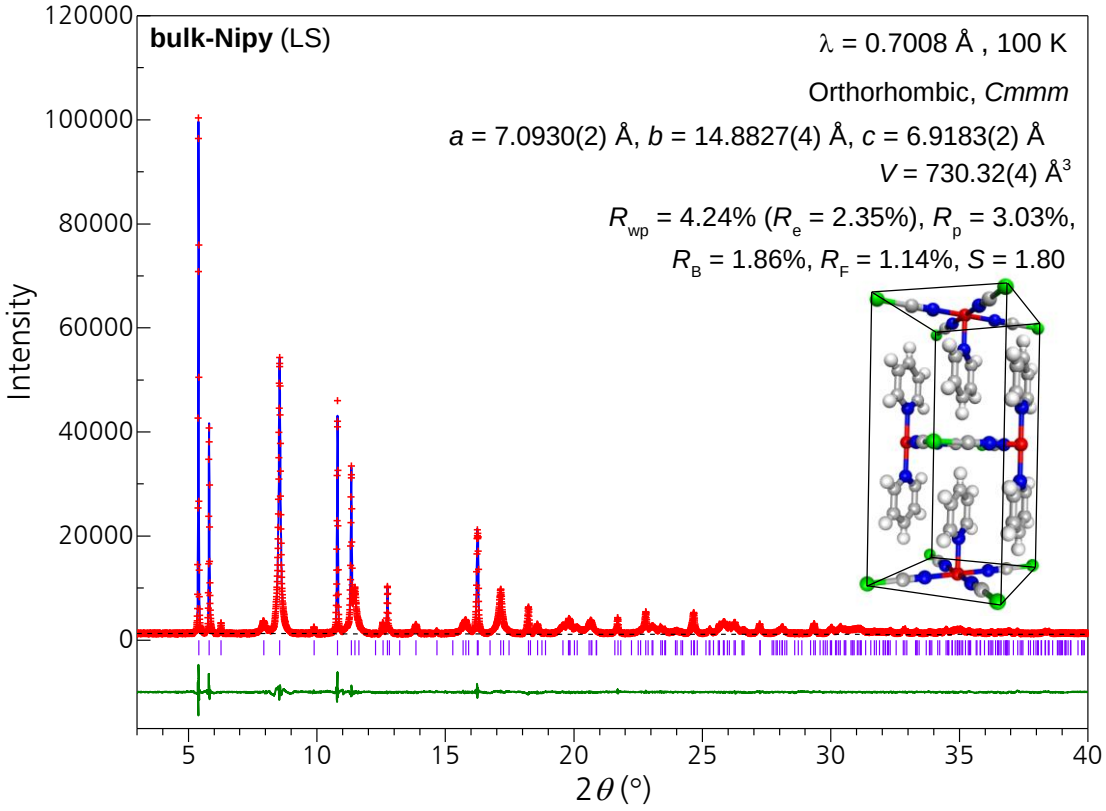

Fig. S2 Rietveld refinement of **bulk-Nipy** structure in LS state. Synchrotron XRD profile of **bulk-Nipy** (red cross) was collected at 100 K. A calculated pattern is represented by a blue line with a background (black dashed line). Magenta bars denote the positions of allowed Bragg reflections. The residual curve (observed minus calculated) is plotted by the below green line. The refined lattice parameters and standard deviations were determined as a = 7.0930(2) Å, b = 14.8827(4) Å, c = 6.9183(2) Å, V = 730.32(4) Å^3. (Inset) A perspective view of the unit cell is shown (orthorhombic, *Cmmm*). Colour code: Fe (red), C (grey), N (blue), Ni (green), H (white).

Table S2 Atomic coordinates and displacement factors for **bulk-Nipy** in LS state (*T* = 100 K).

Atom	Wyckoff position	x	y	z	Site occupancy	U_{iso}
Fe1	2*c*	1/2	1	1/2	1	0.0038
Ni1	2*a*	1	1	1	1	0.0038
N1	8*o*	0.6945(8)	1	0.6898(8)	1	0.00887
N2	4*j*	1/2	0.8645(6)	1/2	1	0.00887
C1	8*o*	0.8180(7)	1	0.8084(8)	1	0.00887
C2	8*n*	1/2	0.8187(4)	0.329(1)	1	0.00887
C3	8*n*	1/2	0.7250(6)	0.329(1)	1	0.00887
C4	4*j*	1/2	0.6788(7)	1/2	1	0.00887
H1	8*n*	1/2	0.849(4)	0.216(5)	1	0.01064
H2	8*n*	1/2	0.695(4)	0.216(5)	1	0.01064
H3	4*j*	1/2	0.616(6)	1/2	1	0.01064

Table S3 Selected bond length [Å] and angle [°] changes in **bulk-Mpy** (M = Ni, Pt) by spin transition. Fe–$N_{pyridine}$ bond length changes upon spin transition in **bulk-Mpy** (M = Ni, Pt) were similar to those of other Hofmann-like MOFs (*ca*. 0.2 Å). For **bulk-Nipy**, the [FeN_6] core in LS state was close to a regular octahedron with angles of 180° for Fe–$N_{cyanide}$–C and 90° for $N_{cyanide}$–Fe–$N_{pyridine}$. A 2D infinite layer of Fe[$Ni(CN)_4$] in HS state was corrugated to show the distorted bond angles 166° and 89°, respectively.

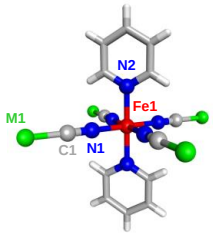

	bulk-Nipy		bulk-Ptpy	
	298 K[16b]	100 K	298 K[15c]	100 K[15e]
Fe1–N1	2.155	1.905(5)	2.159(5)	1.87(1)
Fe1–N2	2.208	2.017(9)	2.2096(16)	2.04(2)
C1–M1	1.861	1.851(5)	1.971(6)	2.04(1)
Fe1–N1–C1	166.2	179.6(6)	179.4(5)	180(3)
N1–C1–M1	176.8	177.4(6)	179.6(5)	180(3)
N1–Fe1–N2	88.8	90	89.84(16)	90

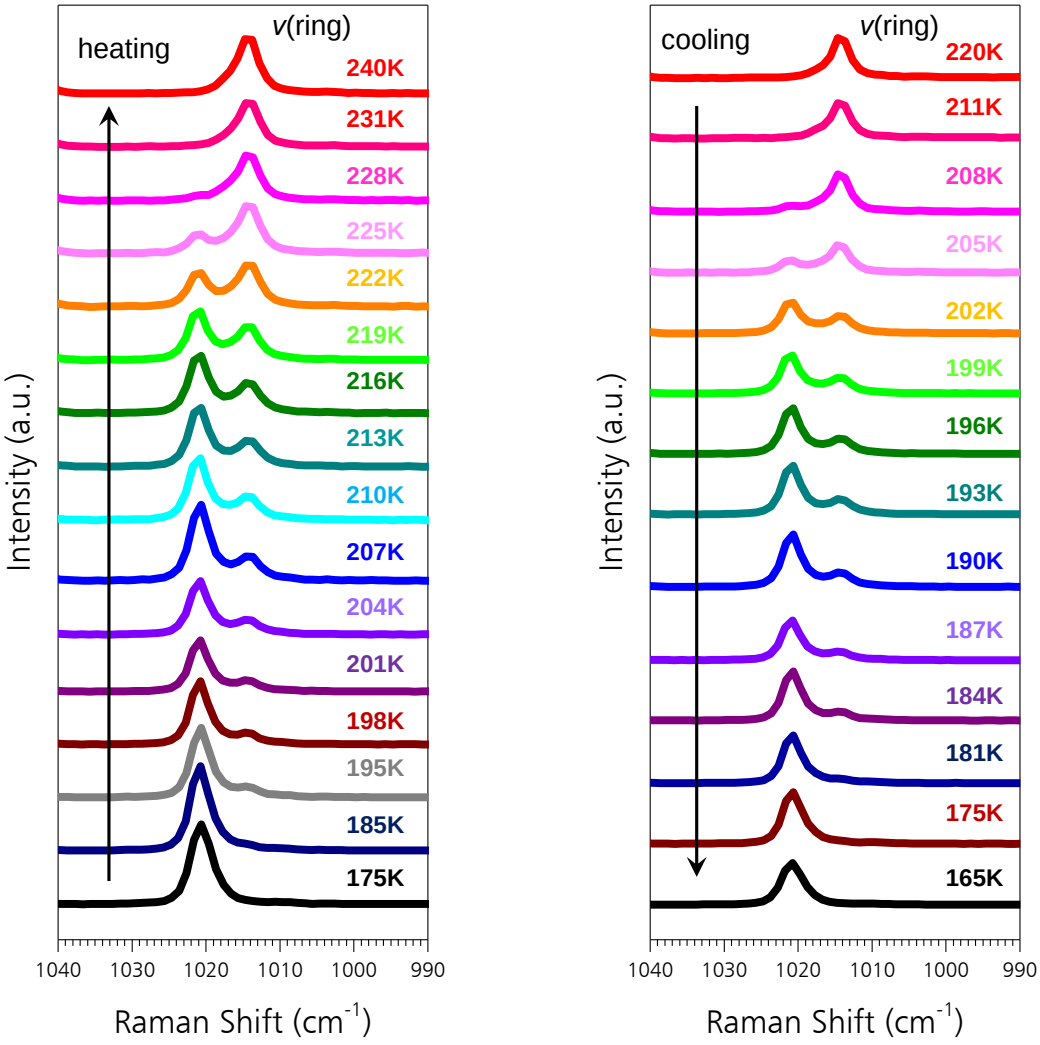

Fig. S3 Variable-temperature Raman spectra of **bulk-Nipy** for (left) heating and (right) cooling steps.

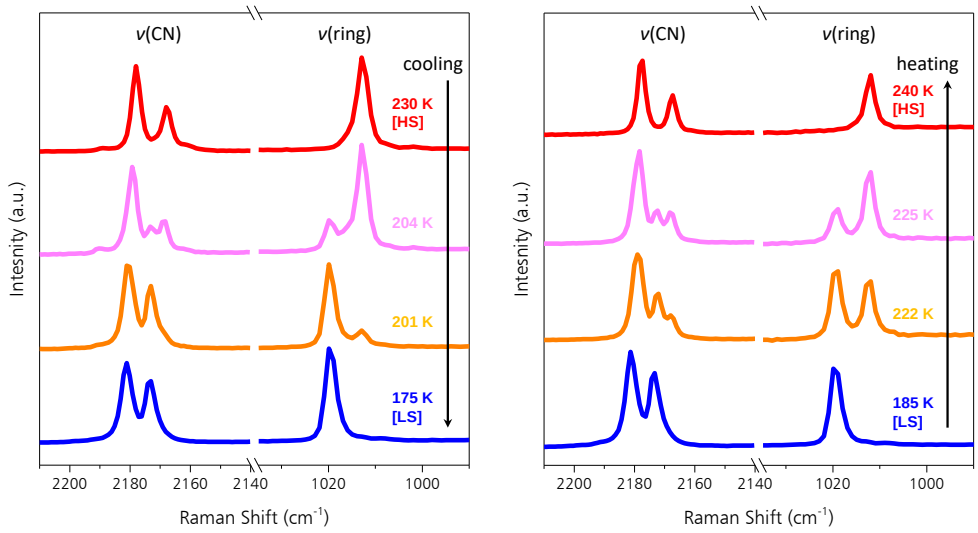

Fig. S4 Spin-state monitoring of **bulk-Nipy** using cyanide stretching modes around the hysteresis region. The vibration modes of the cyanide group in a 2D sheet can also be used to monitor the spin-state change in (left) cooling and (right) heating steps. Spectra from the ring vibration mode were simultaneously collected to compare the peak change in both regions. Observed bands at 2172 cm^{-1} (2167 cm^{-1}) and at 2180 cm^{-1} (2176 cm^{-1}) were assigned to the symmetric and asymmetric stretching modes in the LS (HS) state.

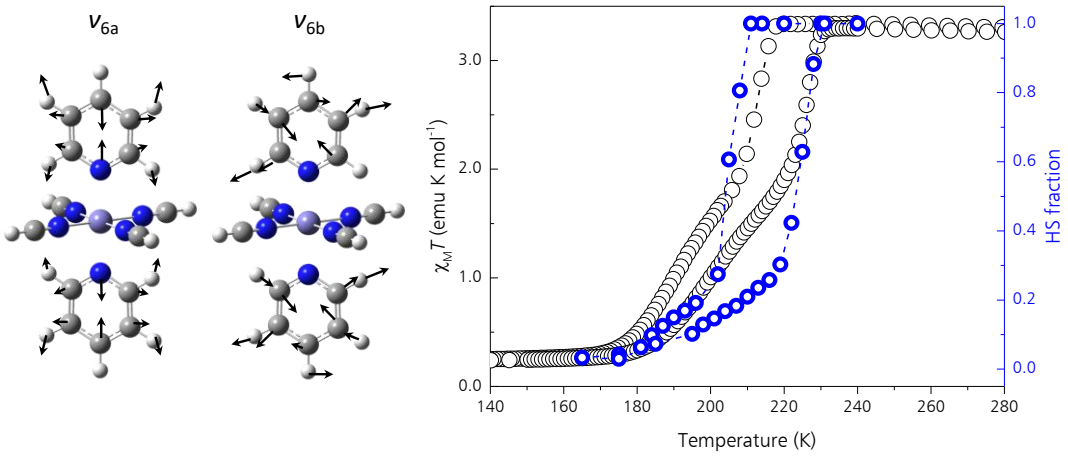

Fig. S5 Temperature dependence of HS fraction in **bulk-Nipy** monitored using another marker of spin state. (Left) In-plane deformation modes ν_{6a} at 642 cm^{-1} and ν_{6b} at 654 cm^{-1} were used as markers for spin states. Black arrows denote atom displacement vectors. (Right) Spin-state monitoring by magnetic susceptibility measurement (black unfilled circle, left axis) and Raman spectroscopy using the markers (blue unfilled circle, right axis).

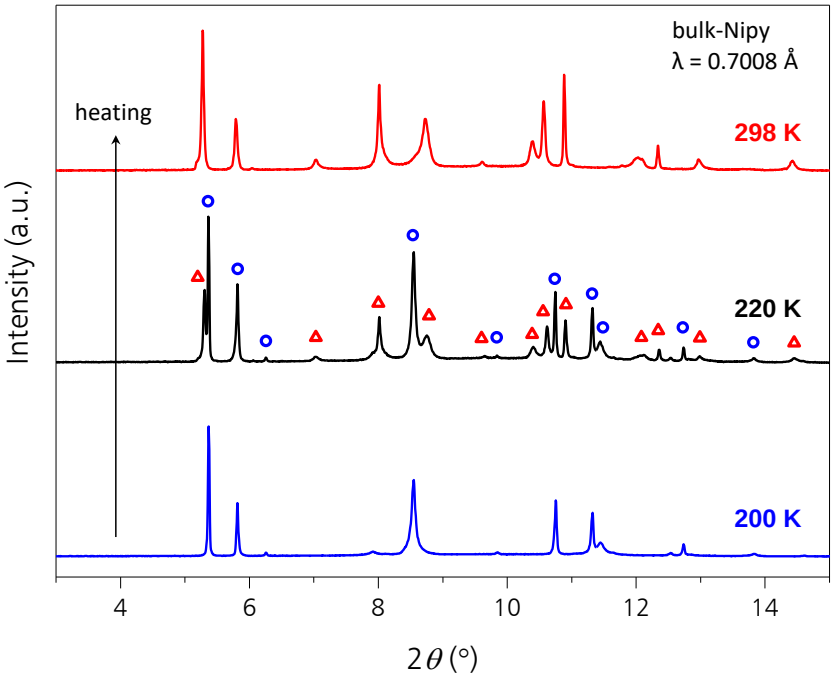

Fig. S6 Variable-temperature XRD measurements for **bulk-Nipy** in the heating step from LS state (at 200 K, blue) to HS state (at 298 K, red). At the middle of the LS–HS transition, 220 K (see Fig. 1c), the diffraction pattern (black line) is a superposition of the patterns of HS (red triangle) and LS states (blue circle). No superstructure (unit cell doubling with nonequivalent Fe^{II} sites) is shown. These observations indicate that the intermediate state in **bulk-Nipy** is a mixing of HS and LS state domains without long-range order.

Table S4 Summary profile of **film-Nipy** samples compared with **bulk-Nipy**. Lattice parameters are represented for **film-Nipy** on as-supplied/annealed Au substrate at rt (see Fig. S19 and S20), **bulk-Nipy** in LS state (at 100 K, Fig. S2) and HS state (at 298 K, Fig. S1), respectively.

	20L (as-supplied)	**40L** (as-supplied)	**20L** (annealed)	**40L** (annealed)	**bulk (LS)**	**bulk (HS)**
Cycle number	20	40	20	40	–	–
Domain size [nm]	12	17	23	28	–	–
a [Å]	15.27(1)	15.26(2)	15.26(4)	15.21(3)	7.0930(2)	15.5290(1)
b [Å]	7.327(4)	7.298(8)	7.18(1)	7.19(1)	14.8827(4)	7.39034(5)
c [Å]	7.174(7)	7.12(1)	7.14(2)	7.15(1)	6.9183(2)	7.0655(1)
β [°]	91.9(4)	91.4(6)	90(1)	90.4(9)	90	101.321(1)
V [Å^3]	802(1)	793(2)	783(4)	783(2)	730.32(4)	795.09(1)
$T_{1/2}^{down}$ [K]	175	187	—		205	
$T_{1/2}^{up}$ [K]	180	187	—		217	

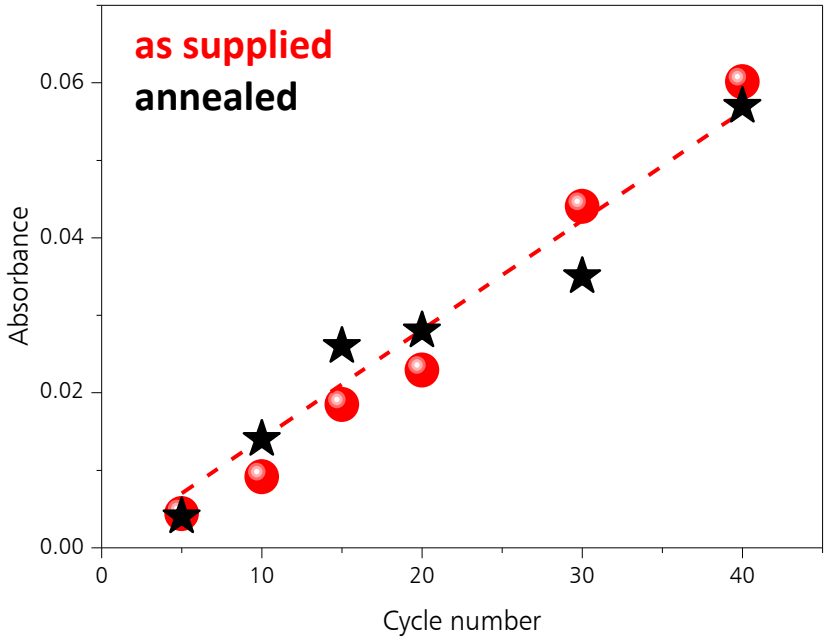

Fig. S7 IRRAS monitoring of LbL crystal growth. The absorbance of *ν*(CN) stretching mode vs. cycle number plots are shown for **film-Nipy** onto as-supplied (red) and annealed Au substrate (black). Red dashed line is the result of linear fitting for data of as-supplied ones.

40L annealed

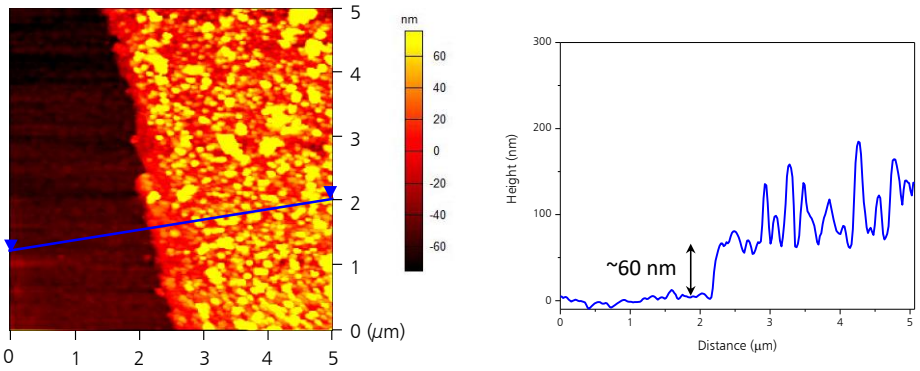

40L as-supplied

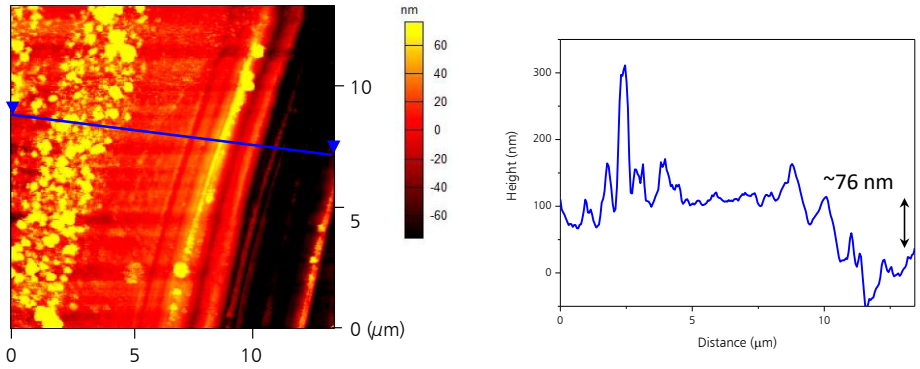

Fig. S8 AFM line profiles for **film-Nipy-40L** onto (upper) annealed and (bottom) as-supplied Au substrate. The offset height value with the scratched area being set to 0 nm is plotted versus line distance (represented by blue inverted triangle), indicating a similar film thickness with some locally grown domains.

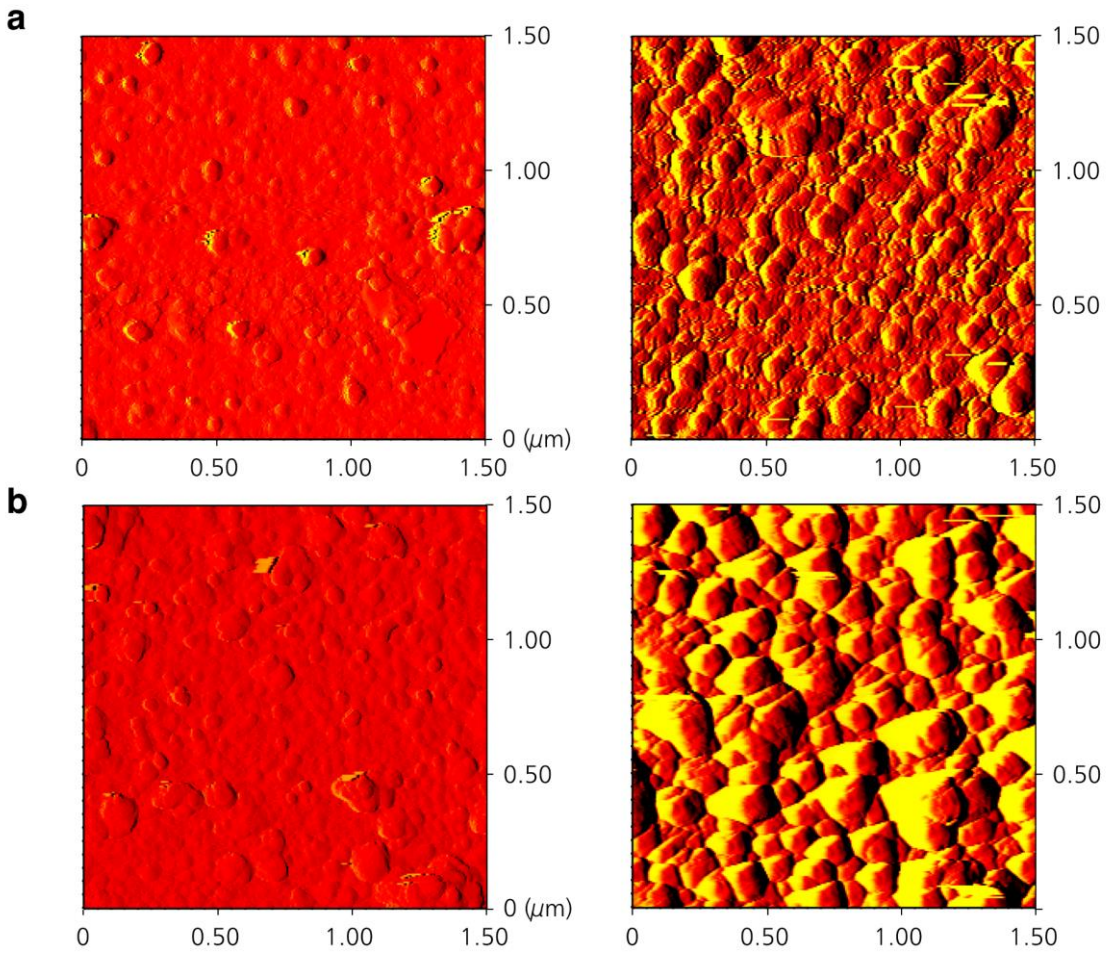

Fig. S9 AFM amplitude images of **film-Nipy**. AFM amplitude images were collected for (a) **film-Nipy-20L** and (b) **film-Nipy-40L** on substrates: (left) as-supplied and (right) annealed Au substrates.

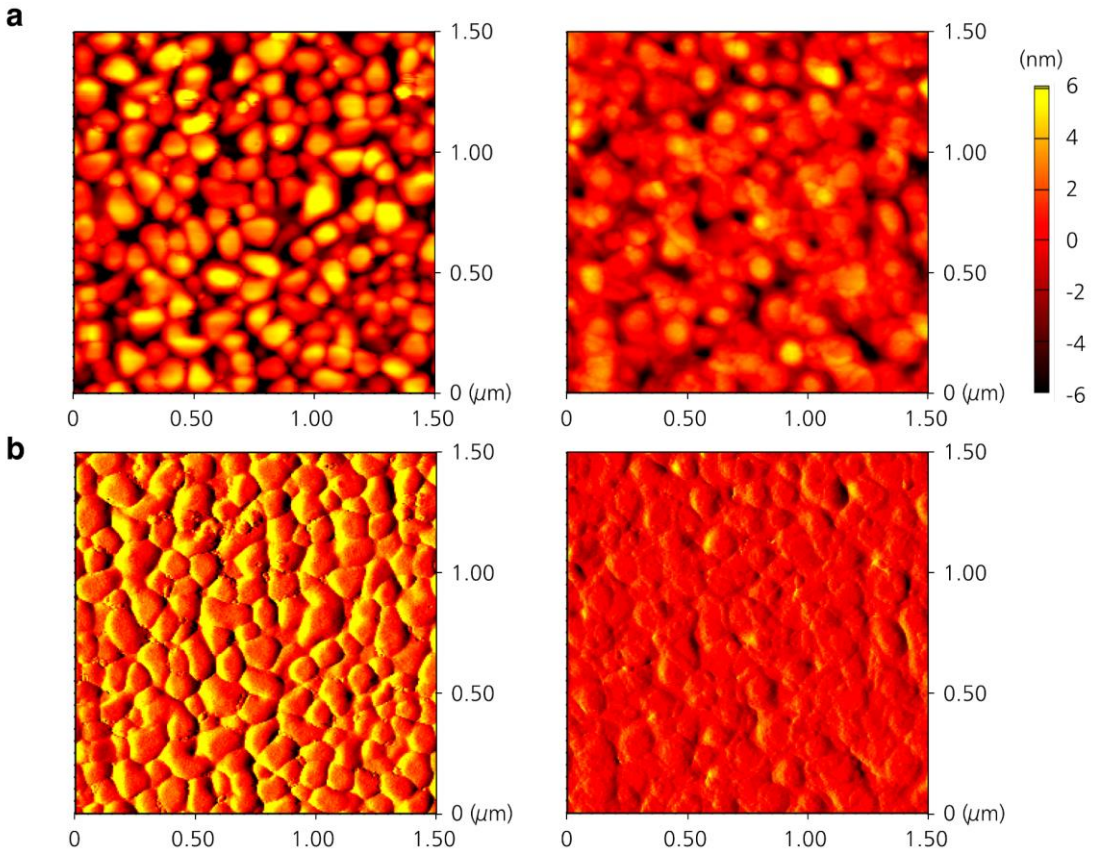

Fig. S10 AFM images of Au substrate. AFM measurements using tapping mode were performed to obtain the following: (a) height image and (b) amplitude image for (left) as-supplied and (right) annealed Au substrates.

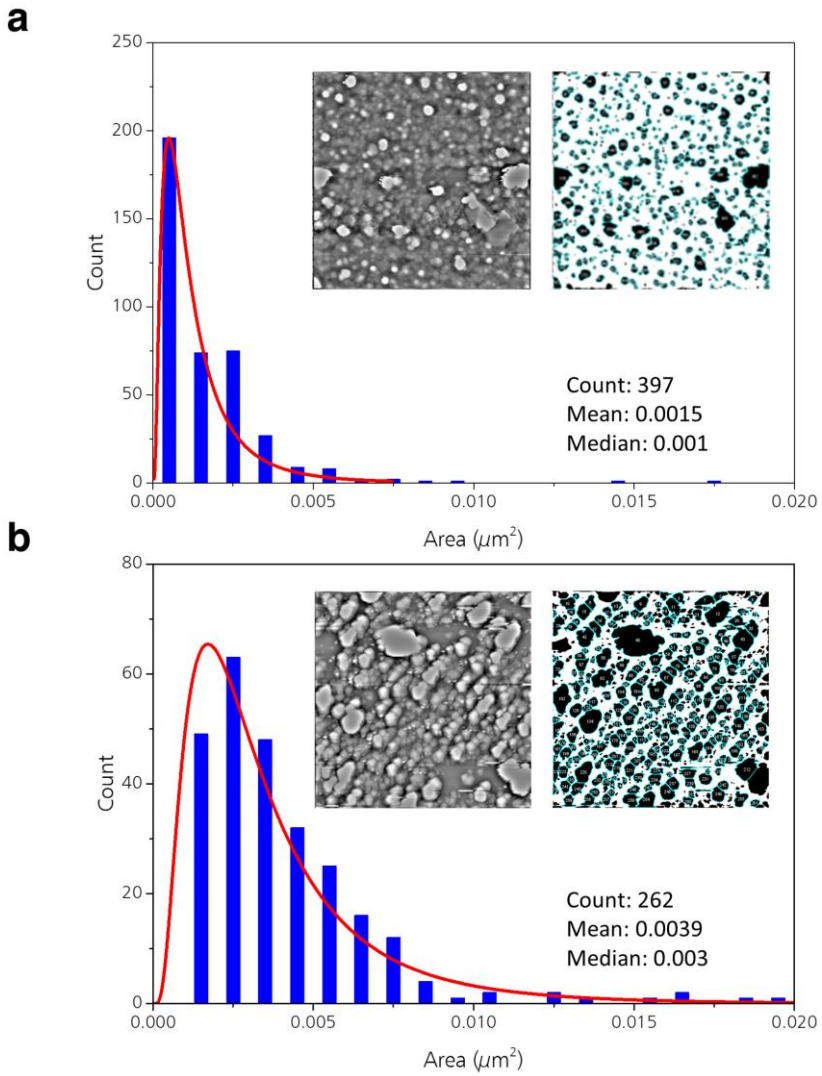

Fig. S11 Domain size distribution of **film-Nipy-20L.** Particle analysis was performed on a binarized image of **film-Nipy-20L** grown on (a) as-supplied and (b) annealed Au substrates. Red lines represent log-normal distribution curves. (Inset) 1.5 × 1.5 μm^2 AFM image after bandpass filter processing and its binarized image for particle analysis.

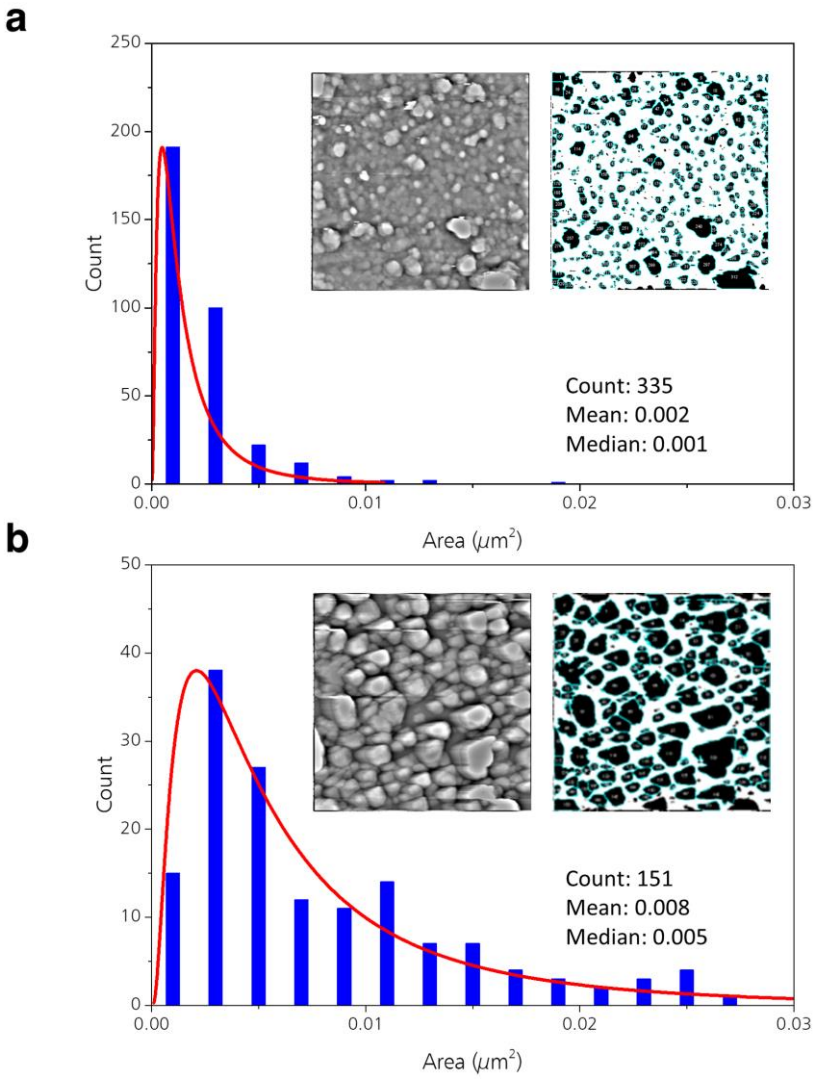

Fig. S12 Domain size distribution of **film-Nipy-40L.** Particle analysis was performed on a binarized image of **film-Nipy-40L** grown on (a) as-supplied and (b) annealed Au substrates. Red lines represent log-normal distribution curves. (Inset) 1.5 × 1.5 μm^2 AFM image after bandpass filter processing and its binarized image for particle analysis.

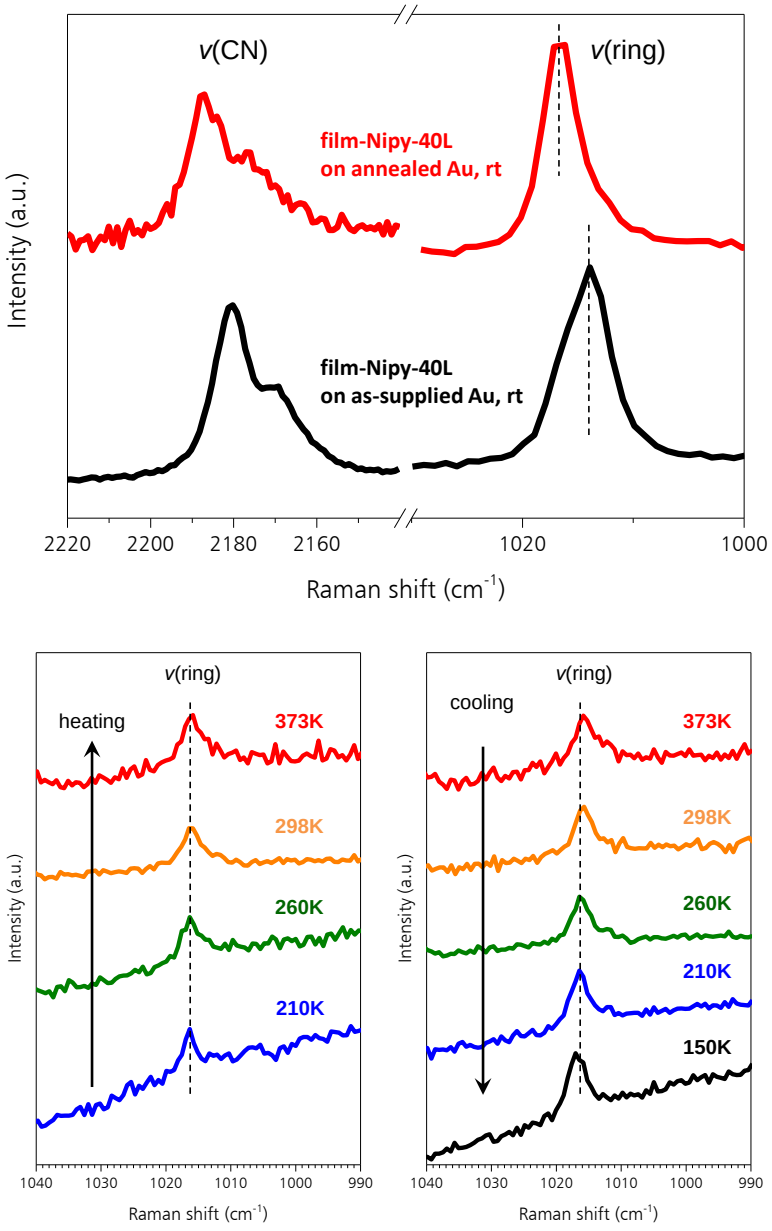

Fig. S13 HS2 state of **film-Nipy-40L** on annealed Au substrate. (Above) Raman spectra of *ν*(CN) and *ν*(ring) modes of **film-Nipy-40L** at rt on (red) annealed and (black) as-supplied Au substrates. Dashed lines represent the difference in the peak positions of HS and HS2 states. (Below) Variable temperature Raman spectra of **film-Nipy-40L** on annealed Au substrate.

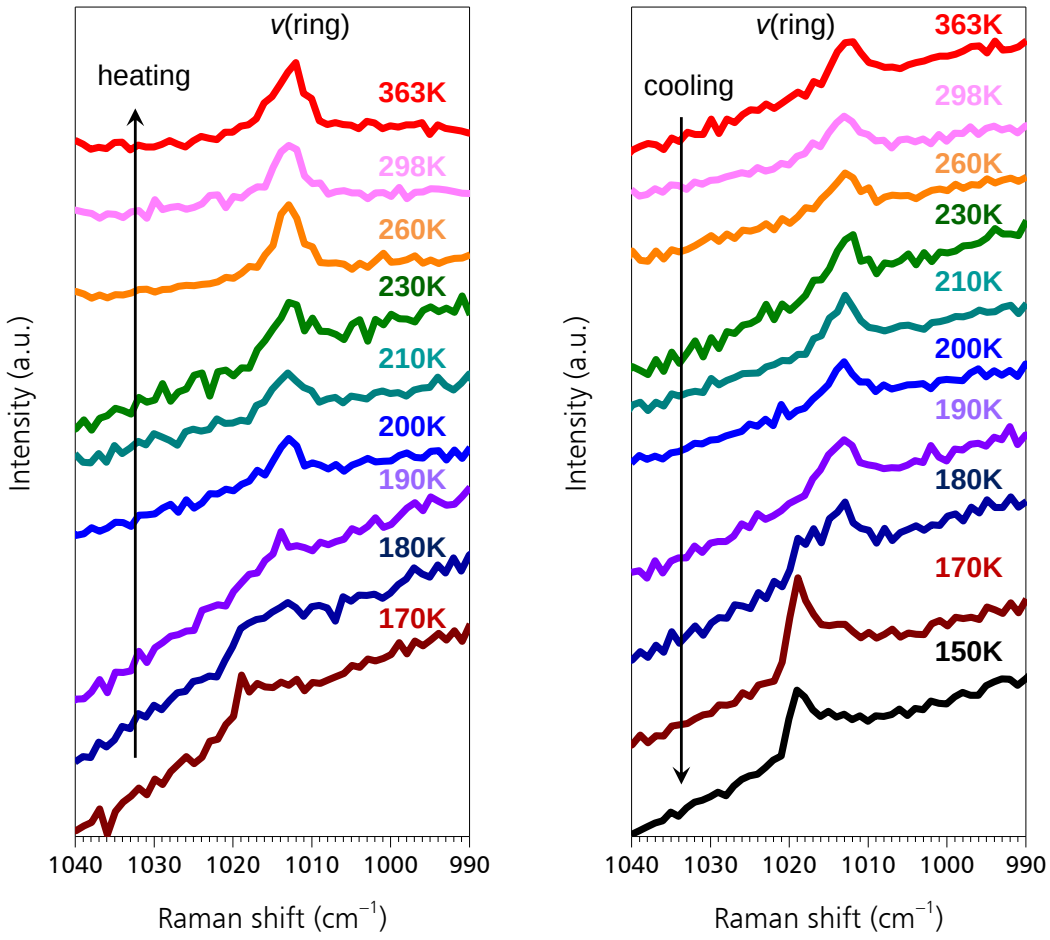

Fig. S14 Variable-temperature Raman spectra of **film-Nipy-20L** on as-supplied Au substrate for (left) heating and (right) cooling steps.

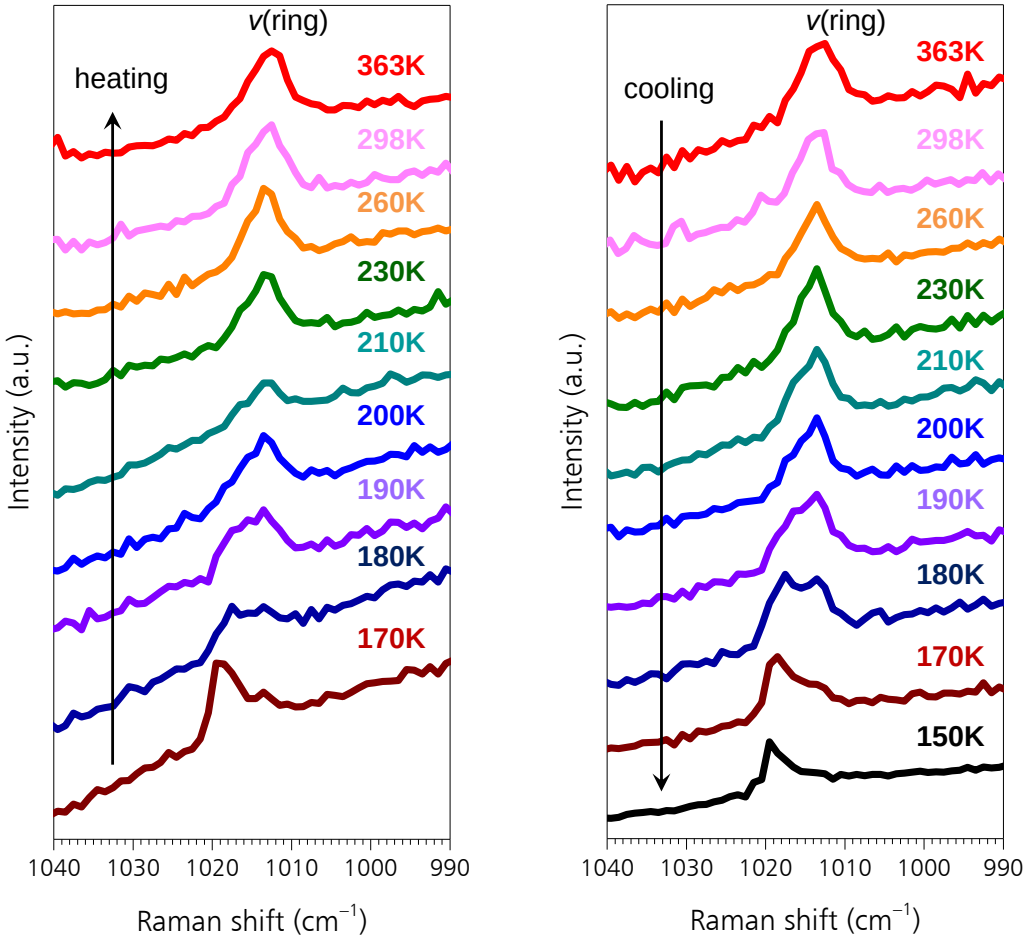

Fig. S15 Variable-temperature Raman spectra of **film-Nipy-40L** on as-supplied Au substrate for (left) heating and (right) cooling steps.

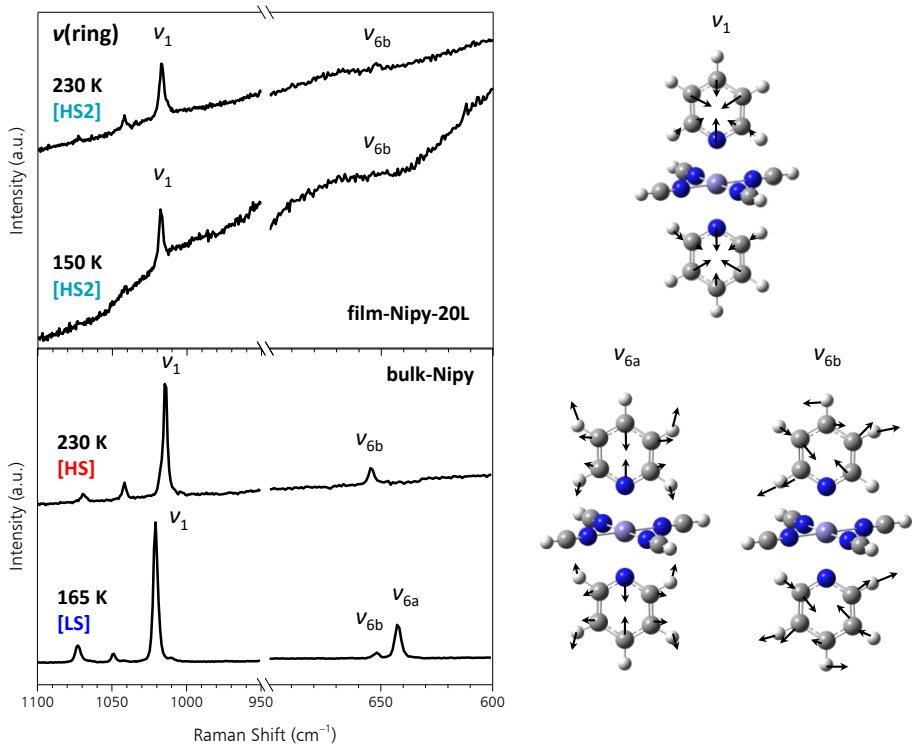

Fig. S16 Variable-temperature Raman spectra of the pyridine ring vibration modes. (Left) Raman spectra of **film-Nipy-20L** on annealed Au substrate and **bulk-Nipy**. (Right) Ring stretching modes with the displacement vector (black arrows) obtained by DFT optimization and frequency calculations.

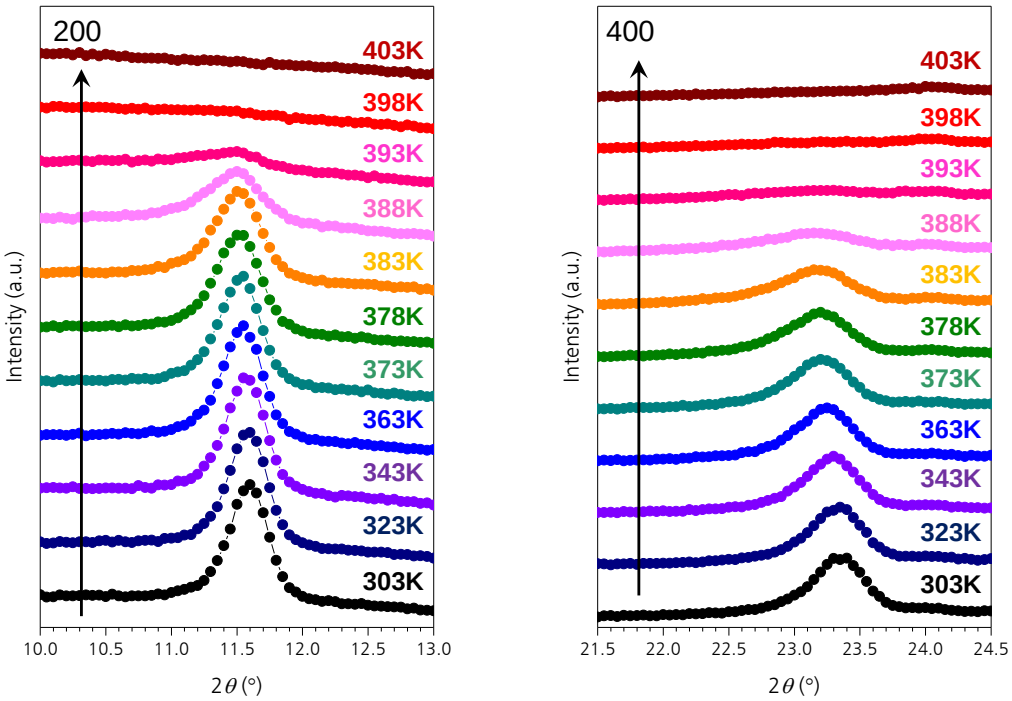

Fig. S17 Thermal stability of **film-Nipy-20L** in HS2 state. Variable-temperature XRD patterns for out-of-plane geometry measured in the (left) 200 and (right) 400 regions. The peak position was shifted slightly lower, indicating thermal lattice expansion upon heating. Thin-film decomposition occurred at about 388–398 K, as confirmed by the absence of diffraction peaks.

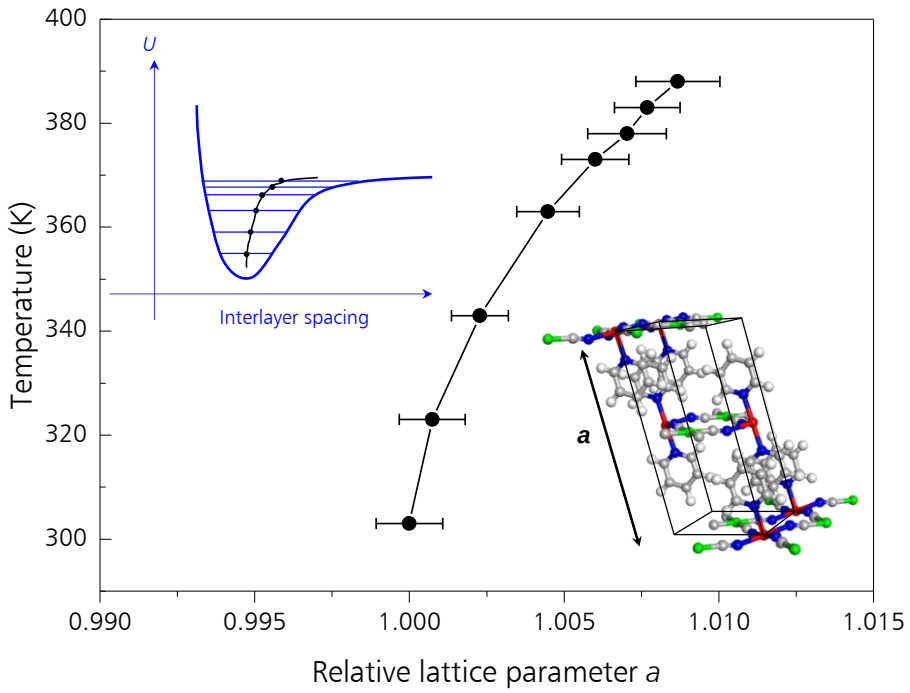

Fig. S18 Thermal-induced interlayer spacing change in **film-Nipy-20L** in HS2 state. The plot of temperature vs. calculated lattice constant a (normalized at 300 K) shows a subtle lattice expansion (0.7% at 383 K). X-axis error bars denote standard deviation using 200 and 400 diffraction peaks. (Inset) (Left) Thermal lattice expansion indicates anharmonicity in a potential energy surface. An equilibrium interlayer spacing is represented by a filled circle. (Right) Unit cell of **bulk-Nipy** in HS state. Colour code: C (grey), N (blue), Fe (red), Ni (green), H (white).

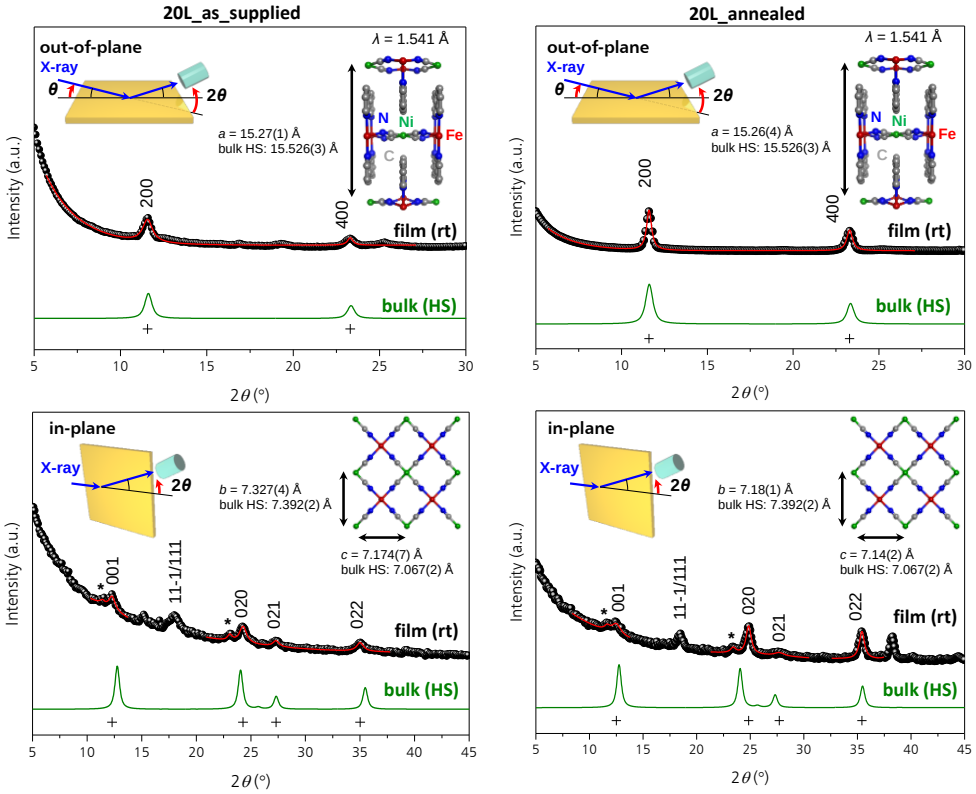

Fig. S19 Surface XRD profiles of **film-Nipy-20L**. Periodic structures of **film-Nipy-20L** on (left) as-supplied and (right) annealed Au substrate at rt characterized by surface XRD measurements for (upper) out-of-plane and (bottom) in-plane geometries. Lattice parameters were determined using observed data (black), fitting results (red), simulated patterns from **bulk-Nipy** in HS state (green) and Bragg reflections (black cross). *200 and 400 diffraction peaks were observed.

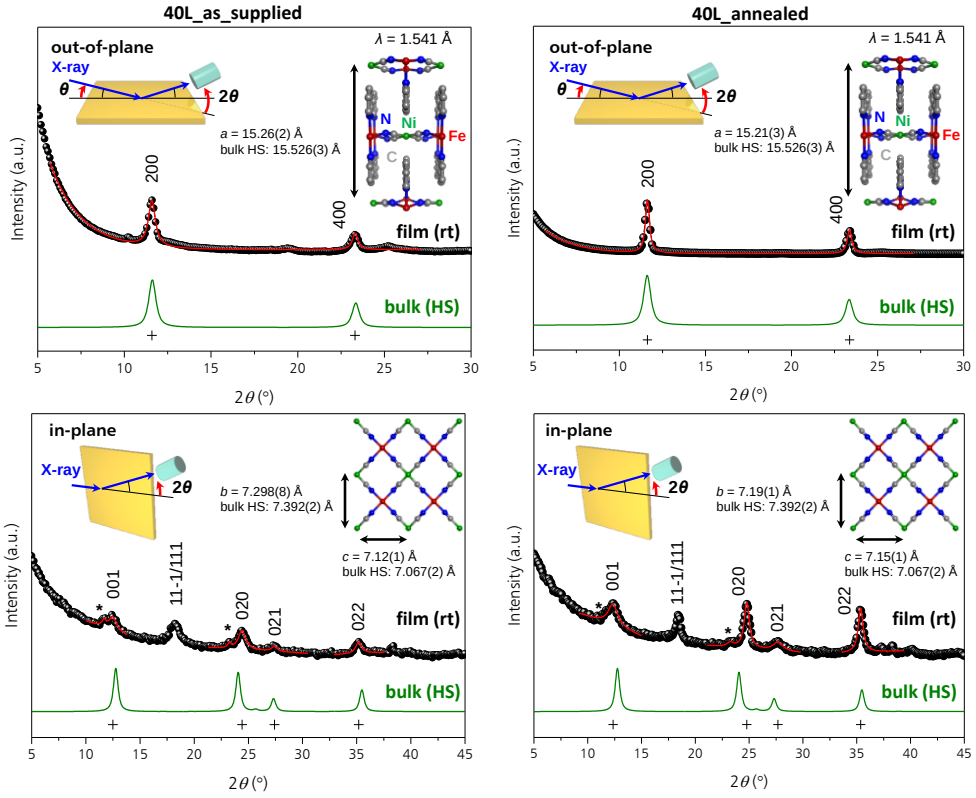

Fig. S20 Surface XRD profiles of **film-Nipy-40L**. Periodic structures of **film-Nipy-40L** on (left) as-supplied and (right) annealed Au substrate at rt characterized by surface XRD measurements for (upper) out-of-plane and (bottom) in-plane geometries. Lattice parameters were determined using observed data (black), fitting results (red), simulated patterns from **bulk-Nipy** in HS state (green) and Bragg reflections (black cross). *200 and 400 diffraction peaks were observed.

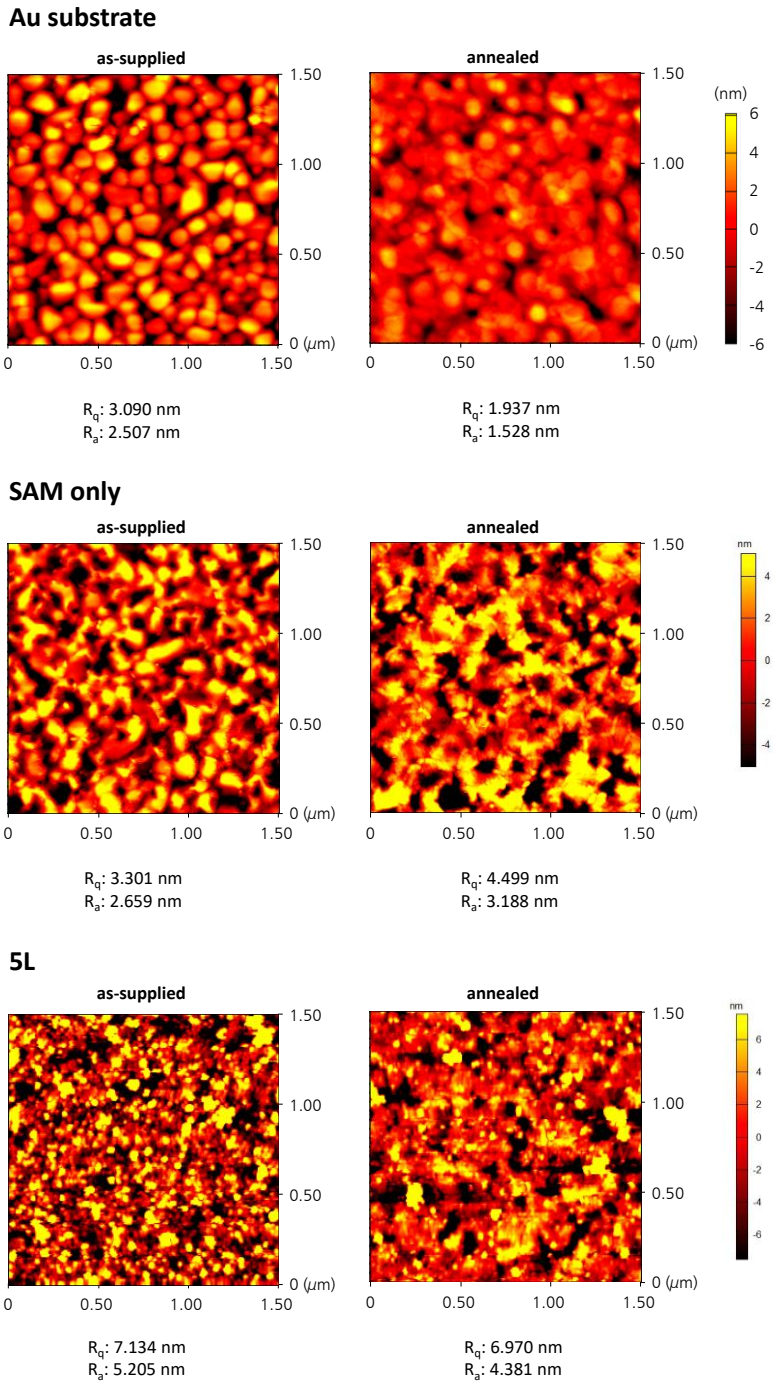

Fig. S21 Surface roughness analysis for **film-Nipy** samples in the early stage of crystal growth. The RMS roughness (Rq, obtained by squaring each height value, then taking the square root of the mean) and average surface roughness (Ra, average deviation from the mean line) are shown for each height image.

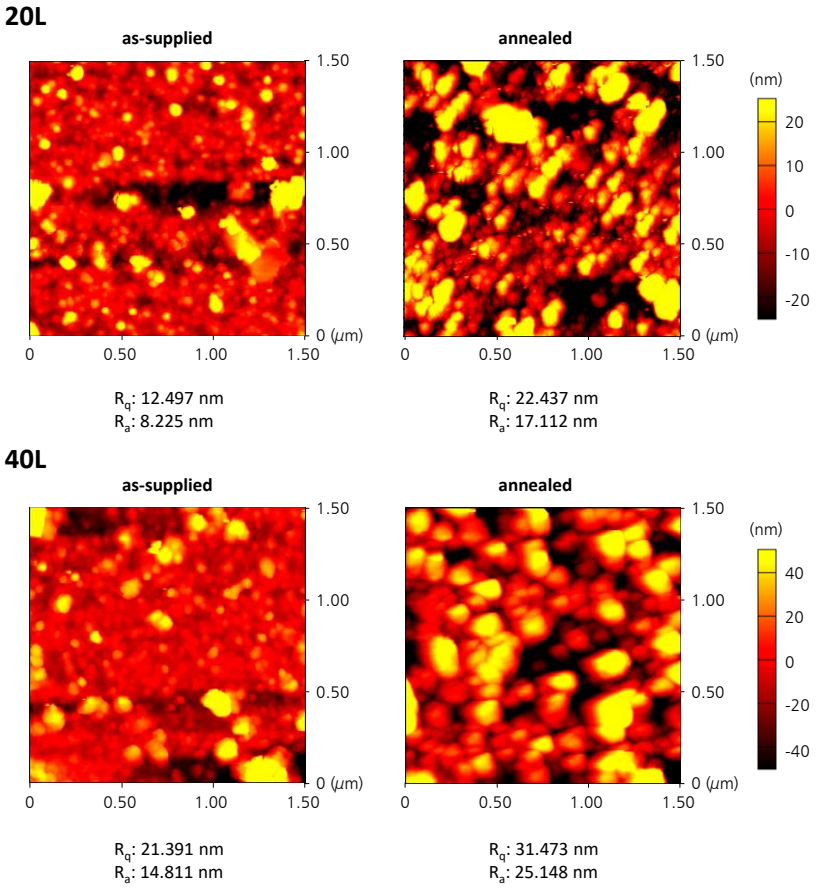

Fig. S22 Surface roughness analysis for **film-Nipy-20L** and **film-Nipy-40L**. Deposition of **film-Nipy** on annealed substrate result in higher surface roughness due to its large crystal size. The surface roughness parameters Rq and Ra are shown for each height image.

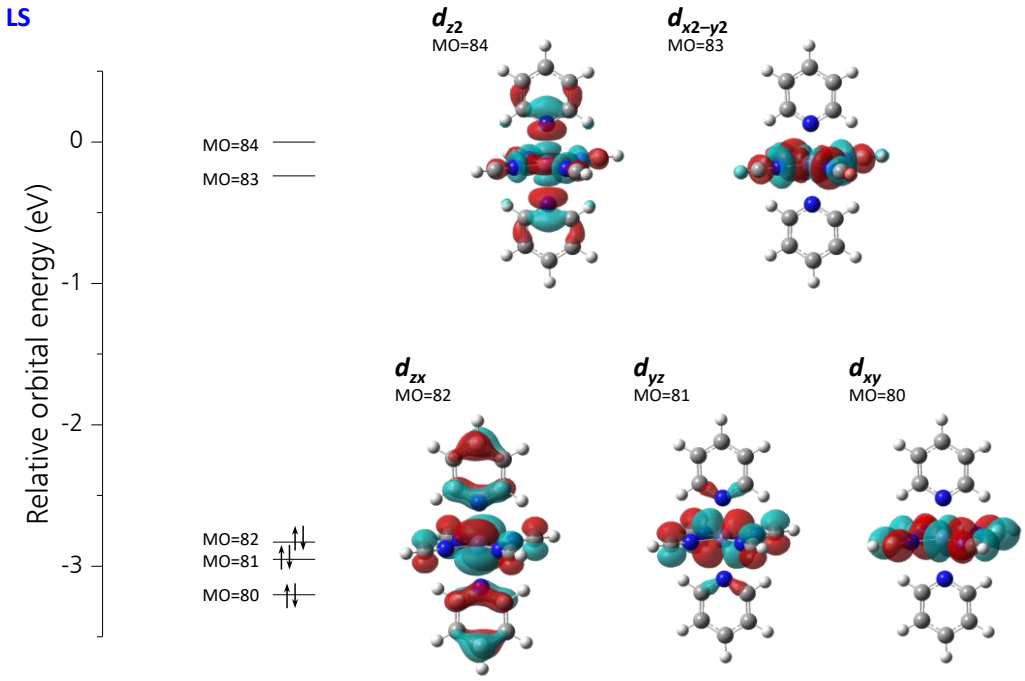

Fig. S23 Molecular orbitals in the energy diagram for the optimized structure of $Fe(py)_2(HCN)_4$ in LS state. In the optimization, $Fe–N_{pyridine}$ and $Fe–N_{cyanide}$ bond lengths were fixed as 2.017 Å and 1.905 Å, respectively. Energy levels are normalized to the energy of the d_{z2} orbital.

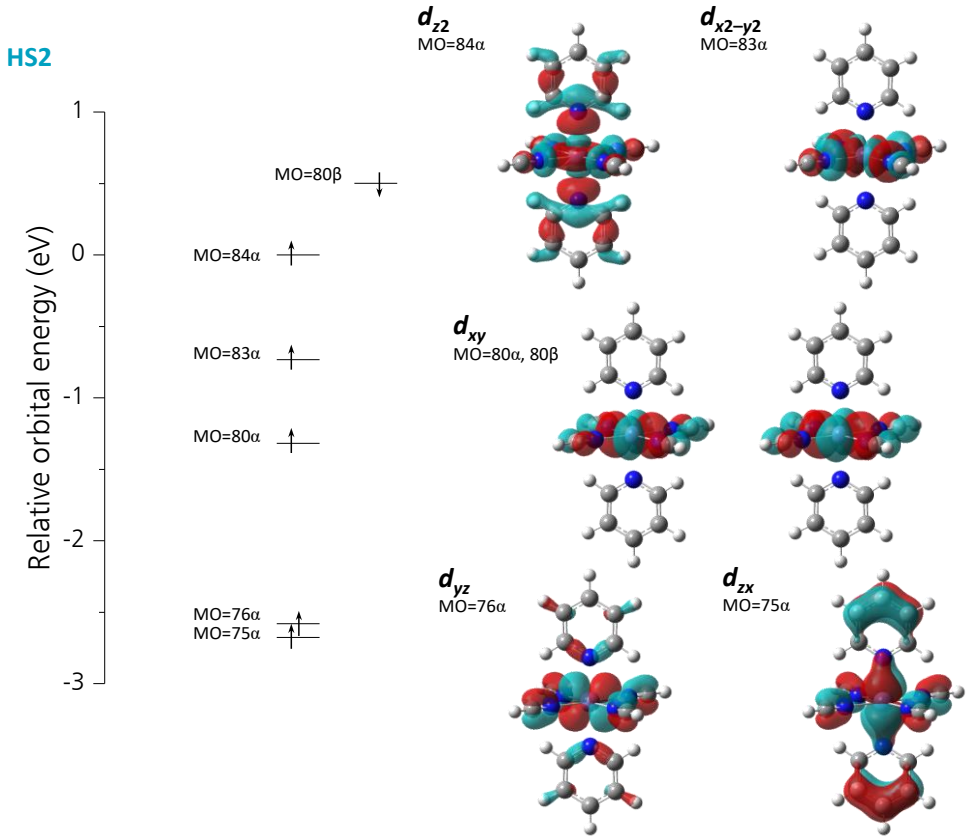

Fig. S24 Molecular orbitals in the energy diagram for the optimized structure of $Fe(py)_2(HCN)_4$ in HS2 state. In the optimization, $Fe–N_{pyridine}$ bond length was fixed as 2.1125 Å (intermediate bond length between those in HS and LS states). The optimized $Fe–N_{cyanide}$ bond length was 2.2065 Å. Energy levels are normalized to the energy of the d_{z2} orbital.

3. Supplementary Notes

24. J. W. Lyons, *Fire*. Scientific American Library, 1985.

25. Y. Huang, H. Qiu, F. Wang, L. Pan, Y. Tian and P. Wu, *Vacuum*, 2003, **71**, 523

26. J. Rundqvist, J. H. Hoh and D. B. Haviland, *J. Colloid Interface Sci*., 2006, **301**, 337.

27. A. Altomare, C. Cuocci, C. Giacovazzo, A. Moliterni, R. Rizzi, N. Corriero and A. Falcicchio, *J. Appl. Cryst.*, 2013, **46**, 1231.

28. F. Izumi and K. Momma, *Solid State Phenom*., 2017, **130**, 15.

29. W. S. Rasband, ImageJ, U. S. National Institutes of Health, Bethesda, Maryland, USA, http://imagej.nih.gov/ij/, 1997–2015.

30. M. J. Frisch, G. W. Trucks, H. B. Schlegel, G. E. Scuseria, M. A. Robb, J. R. Cheeseman, G. Scalmani, V. Barone, B. Mennucci, G. A. Petersson and H. Nakatsuji, *Gaussian 09*, revision D. 01, 2009.